



Structured type III radio bursts observed in interplanetary space

Immanuel Christopher Jebaraj, Athanasios Kouloumvakos, Nina Dresing, V. Krasnoselskikh, Alexander Warmuth, Nicolas Wijsen, S. Poedts, Christian Palmroos, Jan Gieseler, Rami Vainio, et al.

► To cite this version:

Immanuel Christopher Jebaraj, Athanasios Kouloumvakos, Nina Dresing, V. Krasnoselskikh, Alexander Warmuth, et al.. Structured type III radio bursts observed in interplanetary space. *Astronomy and Astrophysics - A&A*, 2023, 670, pp.A20. 10.1051/0004-6361/202243494 . hal-03815538

HAL Id: hal-03815538

<https://hal.science/hal-03815538>

Submitted on 10 Nov 2023




HAL is a multi-disciplinary open access archive for the deposit and dissemination of scientific research documents, whether they are published or not. The documents may come from teaching and research institutions in France or abroad, or from public or private research centers.

L'archive ouverte pluridisciplinaire **HAL**, est destinée au dépôt et à la diffusion de documents scientifiques de niveau recherche, publiés ou non, émanant des établissements d'enseignement et de recherche français ou étrangers, des laboratoires publics ou privés.



Distributed under a Creative Commons Attribution 4.0 International License

Structured type III radio bursts observed in interplanetary space

I. C. Jebaraj^{1,2} , J. Magdalenic^{1,2}, V. Krasnoselskikh^{3,4} , V. Krupar^{5,6}, and S. Poedts^{2,7} 

¹ Solar-Terrestrial Centre of Excellence – SIDC, Royal Observatory of Belgium, Avenue Circulaire 3, 1180 Uccle, Belgium
e-mail: immanuel.c.jebaraj@gmail.com

² Center for mathematical Plasma Astrophysics, Department of Mathematics, KU Leuven, Celestijnenlaan 200B, 3001 Leuven, Belgium

³ LPC2E/CNRS, UMR 7328, 3A avenue de la Recherche Scientifique, 45071 Orléans, France

⁴ Space Sciences Laboratory, University of California, Berkeley, CA 94720, USA

⁵ Goddard Planetary Heliophysics Institute, University of Maryland, Baltimore County, Baltimore, MD 21250, USA

⁶ Heliospheric Physics Laboratory, Heliophysics Division, NASA Goddard Space Flight Center, Greenbelt, MD 20771, USA

⁷ Institute of Physics, University of Maria Curie-Skłodowska, ul. Radziszewskiego 10, 20-031 Lublin, Poland

Received 7 March 2022 / Accepted 25 November 2022

ABSTRACT

Context. The last few decades have seen numerous studies dedicated to fine structures of type III radio bursts observed in the meter–decameter wavelengths. Most of the explanations of the structured radio emission involve the propagation of electron beams through the strongly inhomogeneous plasma in the low corona. To date, only a few type III bursts with fine structures, observed at hecto–kilometric wavelengths, have been reported.

Aims. We report here the existence of numerous structured type III radio bursts observed during the STEREO era by all three WAVES instruments on board STEREO A, B, and Wind. The aim of the study is to report and classify structured type III bursts, and to present the characteristics of their fine structures. The final goal is to try to understand the physical mechanism responsible for the generation of structured radio emission.

Methods. In this study we used data from all available spacecraft, specifically STEREO and Wind. We employed 1D density models to obtain the speed of the source of type III radio emission, the electron beam. We also performed a spectral analysis of the fine structures in order to compare their characteristics with the metric–decametric fine structures.

Results. The presented similarities of the type III fine structures in the metric to decametric and interplanetary wavelengths indicate that the physical processes responsible for the generation of structured type III radio bursts could be the same, at heights from the low corona to the interplanetary range. We show that the observed structuring and intermittent nature of the type III bursts can be explained by the variation in the level of density fluctuations, at different distances from the Sun.

Key words. radiation mechanisms: non-thermal – Sun: radio radiation – Sun: activity – waves – turbulence – Sun: general

1. Introduction

Type III radio bursts are among the most intense radio emissions of solar origin. They are also frequently observed, by both space-based and ground-based radio observatories. They are the radio signatures of suprathermal electron beams propagating along open and quasi-open magnetic field lines. In a dynamic radio spectra (color-coded frequency–time diagrams) type III bursts are recorded as fast drifting bursts appearing at a wide range of frequencies almost simultaneously (see e.g. [Suzuki & Dulk 1985](#), for review). Along with type II radio bursts which are the radio signatures of shock waves propagating in the solar corona, type III radio bursts are the most studied solar radio bursts because they can provide information about the associated eruptive events and the ambient plasma conditions.

Solar radio bursts are observed at decreasing frequencies as the associated radio source propagates away from the Sun. In the metric to decametric wavelengths (300–20 MHz), radio emission can be studied using both, dynamic spectra and interferometric observations (see e.g. [Magdalenic et al. 2010](#); [Zucca et al. 2014](#); [Kontar et al. 2017](#); [Sharykin et al. 2018](#)). These two types of observations provide complementary information about the radio bursts, i.e. the shape and extent of radio bursts and the

position of associated radio sources projected in the plane of the sky. Due to the ionospheric cutoff ([Erickson 1997](#)), radio emission beyond ≈ 20 MHz is only observed by some ground-based instruments (e.g. [Melnik et al. 2018](#)).

Space-based radio observations start at frequencies of about 10 MHz, and radio bursts observed below 3 MHz (hectometer to kilometer wavelengths) are considered to be interplanetary radio emission. Similar to the radio bursts in the metric wavelength range, interplanetary radio bursts are also mostly generated by propagating shock waves (type II bursts, [Krasnoselskikh et al. 1985](#); [Kouloumvakos et al. 2021](#)) and electron beams traveling along open field lines (type III bursts, [Ginzburg & Zhelezniakov 1958](#)).

Interplanetary radio emission of solar origin is generally considered to be generated by plasma emission mechanism. Bursts are observed at the fundamental of local plasma frequency, its second harmonic, and sometimes at both the fundamental and the second harmonic ([Kellogg 1980](#)). Although the fundamental emission is dominant, the harmonic plasma emission is also sometimes observed in interplanetary space (e.g. [Leblanc et al. 1998](#)).

Radio observations in the hectometer to kilometer wavelengths are mostly limited to the dynamic spectra which

show the intensity of emission as a function of frequency and time, but lack spatial information. Sometimes stereoscopic direction-finding observations are also available. In particular, since the launch of STEREO mission, direction-finding observations are continuously provided bringing us the unique opportunity to study the positions of radio sources to better understand the origin of interplanetary radio emission (see e.g. [Martínez Oliveros et al. 2012](#); [Magdalenic et al. 2014](#); [Jebaraj et al. 2020, 2021](#)).

Recent advancements in radio imaging techniques and space-based spectroscopic observations have improved the possibility for the identification, categorization, and analysis of radio fine structures. Extensive reporting and studies are available for metric fine structure (see for e.g. [Bhonsle et al. 1979](#); [Magdalenic et al. 2006, 2020](#)) of different types of radio bursts (types II, III, IV). On the contrary, a very small number of studies report the low frequency radio fine structures (e.g. [Chernov 2011](#); [Pulupa et al. 2020](#); [Chen et al. 2021](#)). Simultaneous observations from the different viewing perspectives provided by the STEREO and Wind spacecraft over the last decade, have provided us with a large database of long wavelength observations revealing a number of different radio fine structures of both type II and type III radio bursts.

In this study we present for the first time, different radio fine structures observed by the Wind/WAVES and STEREO/WAVES instruments. We describe the characteristics and the morphology of interplanetary fine structures and discuss their possible origin. Unfortunately, it was not possible to perform a radio triangulation study (e.g. [Magdalenic et al. 2014](#); [Jebaraj et al. 2020](#)) to locate the position of the associated radio sources: many well-observed structured type III bursts reported here were recorded by spacecraft separated by about 180 degrees, which is not favorable for radio triangulation ([Krupar et al. 2016](#)).

This paper is structured as follows. We describe the data and methods used in this analysis in Sect. 2, and give a brief introduction to interplanetary type III radio emission in Sect. 3. We then describe the morphological characteristics of three different classes of interplanetary type III fine structures, namely interplanetary type IIIb bursts (Sect. 3.1), type III bursts with triangular substructures (Sect. 3.2), and type III bursts with irregular fine structures (Sect. 3.3). In Sect. 4, we propose a model for the generation of fine structures and their characteristics. Finally, the summary of our findings and a discussion of the results can be found in Sect. 5.

2. Data and methods

In this study we used observations from WAVES instruments on board the twin spacecrafts, Solar TERrestrial Relations Observatory Ahead and Behind (STEREO A and B [Kaiser 2005](#); [Bougeret et al. 2008](#)), and the Wind spacecraft ([Bougeret et al. 1995](#)). All three WAVES instruments provide intensity-time data at unique frequencies in the form of a radio dynamic spectra. The frequency range we utilized from the STEREO/WAVES instrument is 125–16 000 kHz (HFR receiver only), and from Wind/WAVES 4–13 825 kHz (RAD 1 and RAD 2 receivers).

We started our study by inspecting space-based radio observations for event selection. Once the radio events were identified, we looked for the possibly associated coronal mass ejections (CME)–flare events observed in the low corona by white-light coronagraphs (e.g. STEREO/COR2; [Howard et al. 2008](#)) and extreme-ultraviolet imagers (e.g. STEREO/EUVI; [Howard et al. 2008](#)).

3. Interplanetary type III radio bursts

Of the five main types of plasma radio emissions of solar origin, type III radio bursts are the most frequently observed. Type III radio bursts are generated by beams of suprathermal electrons (a few keVs to tens of keVs) propagating anti-sunward along open and quasi-open magnetic field lines. The broadband emission produced by fast electron beams is observed in dynamic spectra as rapidly drifting bursts (see Fig. 1 and for a review see e.g. [Bhonsle et al. 1979](#), and references therein). Based on their morphology different types of metric to decametric type III bursts were distinguished (see e.g. [Kundu 1965](#); [Bhonsle et al. 1979](#)). Structured type III bursts were frequently reported, but only at meter and decameter wavelengths (e.g. [Chernov et al. 2007](#); [Kontar et al. 2017](#); [Melnik et al. 2018](#)).

For the past 14 years of the STEREO era, numerous hectometric to kilometric type III radio bursts have been observed, and some of which were also structured type III bursts. We report here for the first time report and classify the most frequently observed structured interplanetary type III bursts.

We distinguish three main categories of type III bursts with fine structures: (i) interplanetary type IIIb bursts with and without an envelope, (ii) type III bursts with triangular substructures and (iii) type III bursts with irregular substructures. Table 1 lists the different radio events, addressed in our study, with structured interplanetary type III bursts. We note that the presented events are only selected examples, and larger number of structured type III bursts was found.

3.1. Interplanetary type IIIb bursts

3.1.1. General characteristics

The most frequently observed type III radio bursts with fine structures are the type IIIb bursts. This subcategory of bursts are morphologically very similar to the metric–decametric type IIIb bursts (first reported by [de La Noe & Boischot 1972](#)). The interplanetary type IIIb radio bursts are sometimes associated with eruptive CME–flare events and sometimes only with the complex active regions, similarly to ordinary type III bursts. Although some of the type IIIb bursts are observed at frequencies of up to 1000 kHz they are primarily recorded at frequencies below 700 kHz and then they do not have a high frequency type III counterpart. Of the 12 radio events presented in the Table 1, 6 events consisted of type IIIb bursts.

Despite the observed fine structures, the overall spectral morphology (i.e. the envelope of the interplanetary type IIIb bursts) is similar to that of the classical type III bursts. The same characteristic was also found for the decameter type IIIb bursts ([Ellis & McCulloch 1967](#); [de La Noe & Boischot 1972](#); [Sharykin et al. 2018](#); [Zhang et al. 2020](#)).

The main characteristic of the interplanetary type IIIb bursts is their well-defined substructures, called striae. The stria substructures are generally organized within the type III burst envelope as shown in Figs. 1 and 2. They sometimes show quasi-periodicity (Figs. 1 and 2), and sometimes an irregular pattern (Fig. 3). The frequency bandwidth of the striae was found to be in the range of 70–120 kHz. For comparison, the bandwidth of stria structures observed in the meter to decameter wavelength range varies between 30 and 300 kHz.

In the majority of events the duration of striae is frequency dependent, meaning that the duration of these narrowband structures is longer at lower observing frequencies. However, the

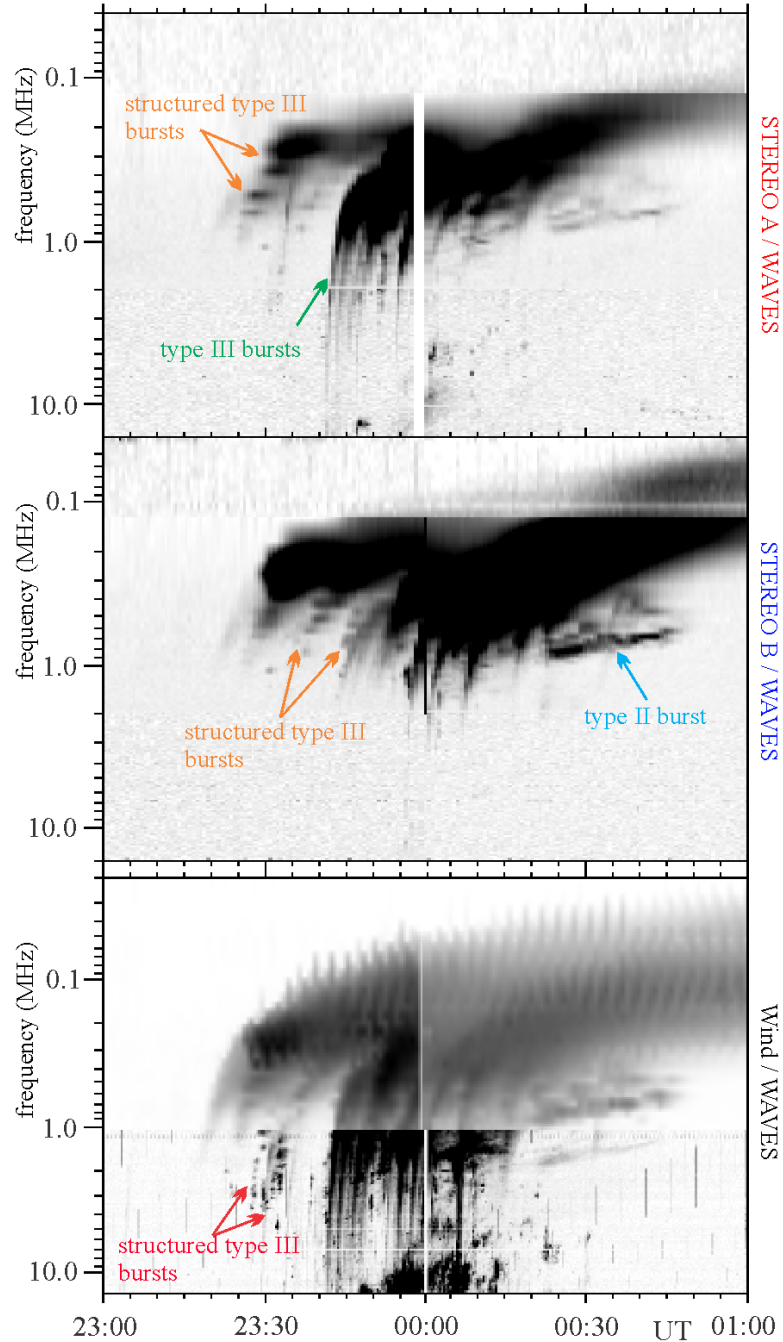


Fig. 1. Complex radio event observed on the evening–early morning of 27–28 September, 2012, showing type II bursts, regular interplanetary type III bursts, and structured type III bursts. The two different types of structured type III bursts are shown in orange and pink.

irregular stria structures, with longer duration at higher frequency, are also occasionally observed (Fig. 3). Their duration is on average between 120 s (at 4000 kHz) and 600 s (at 200 kHz), which is five times longer at five times lower frequency. This regularity in the bandwidth and duration is suggestive of the plasma characteristics necessary for the generation of interplanetary type IIIb bursts.

The envelope of the type IIIb bursts is generally of significantly lower intensity than the substructures of the bursts. Therefore, in most of the studied radio events the dynamic spectrum alone cannot clearly show if the type IIIb envelope exists or not. This is why we also inspected the individual frequency–time profiles of the studied bursts (see Sect. 3.1.1 and Fig. 5).

3.1.2. Examples of type IIIb bursts

Figures 1–4 show different examples of type IIIb bursts. The radio events presented in Figs. 2–4 were associated with the repeated eruptive activity from the complex active regions. Only the radio event observed on 27–28 September, 2012 (Fig. 1) was clearly associated with the CME–flare event studied in detail by Jebaraj et al. (2020). This radio event consists of numerous type III radio bursts, structured type III bursts, and two type II bursts. The structured interplanetary type III bursts were very clearly observed by both twin STEREO spacecraft. The most prominent are the IIIb radio bursts indicated by the orange line in the Fig. 1. The structured radio emission was observed simultaneously by

Table 1. Three classes of type III fine structures observed in interplanetary space.

Type of fine structure	Date	Time	Bandwidth (kHz)	Duration (seconds)	Comment
IP Type IIIb bursts (Figs. 2 and 3)	19/09/2011	06:45, 11:10	60–90	240–600	Most commonly observed type III fine structures in IP space.
	21/11/2011	13:30, 15:00, 16:00	70–100	300–600	Morphological characteristics are somewhat similar to decameter type IIIb.
	22/11/2011	18:10, 19:00, 20:00	70–100	240–600	Exhibit clear structuring and are well separated.
	23/11/2011	10:00, 11:00	120–200	180–660	
	11/12/2011	20:00	60–90	150–450	
	27/09/2012	23:25, 23:25	70–90	240–600	
Triangular striae burst (Fig. 8)	12/11/2010	07:55	90–120	30–300	Rarest type III fine structures. Can also be observed in the higher hectometer wavelengths.
Irregular type IIIb burst (Fig. 11)	12/11/2010	13:45	90–120	60–300	Observed mostly in higher hectometer wavelengths.
	31/07/2011	19:00	50–90	120–160	
	11/08/2011	10:35	30–80	30–120	Have no clear structuring and can occur in irregular intervals.
	22/11/2011	01:20	60–100	120–300	
	30/11/2011	07:50	80–110	60–150	

Notes. The figures showing examples of the studied classes of bursts are also given in the table.

two different instruments, and it is therefore certain that it is not an instrumental effect.

Figure 2 shows several subsequent type III bursts, three of them type IIIb bursts, one type III burst with irregular substructures, and a few ordinary type III bursts. Two type IIIb bursts (at about 13:40 UT and 14:30 UT) could be the structured harmonic emission with the fundamental counterpart observed as regular type III. Similar pairs of type III bursts were already reported in the decameter range (see e.g. Melnik et al. 2018, 2019; Zhang et al. 2020). The type IIIb bursts at about 15:00 UT and 16:00 UT do not show a fundamental-harmonic pair as only structured type IIIb emission was observed. However, the bursts sometimes appear without specific sequence (i.e. we observe that the ordinary type III can be followed by the structured one or vice versa). In such events it is difficult to clearly distinguish whether they make type III–type IIIb pairs, similar to the decametric bursts (Melnik et al. 2018, 2019).

3.1.3. Radio events on 19 September 2011

The radio events on 19 September 2011 exhibit particularly well-observed stria substructures of the type IIIb burst (Figs. 3 and 4) which we discuss here in detail. Figure 3 presents one more radio event on 19 September 2011, observed in the time interval 06:00–07:15 UT. As in the right panel of Fig. 4, we overlaid the one-to-one schematic presentation of fine structures on the dynamic spectrum. The schematic presentation was done on the STEREO A observations in which the bursts were best defined. The different colors indicate fine structures belonging to different bursts. The starting frequency and the intensity of the striae is very similar, practically identical, in both STEREO A and STEREO B observations. Furthermore, the morphologies of the stria substructures, as seen by the two STEREO spacecraft, seem to be almost identical. The one-to-one schematic presentation of striae (Fig. 3, right panel) outlines these similarities in the spectral morphology. Taking into account both the morphology and timing of the structured type IIIb bursts, and assuming that the radio emission is brightest in the direction of its propagation (e.g. Magdalenic et al. 2014; Jebaraj et al. 2020), we can approximate

that the source location of the striae is more or less equidistant for the two spacecraft.

The Wind observations show very faint fine structures with about two orders of magnitude lower intensity than the bursts observed by the twin STEREO spacecraft. Due to low intensity of the bursts, it is not possible to estimate the exact start time of the stria substructures. The detection of type IIIb burst in the Wind observations would be unreliable if not confirmed by STEREO observations. What we can conclude from the Wind observations is that the structuring of the radio emission is not intensity dependent, and striae can also be generated within the very low intensity radio bursts.

The frequency drift rate of the type IIIb burst, estimated along the brightest parts of the stria substructures, is higher than that of the regular type III observed immediately after (at about 06:50 UT). The frequency drift rate of the type IIIb burst is 14 kHz s^{-1} in the range 1000–500 kHz (which corresponds to $\approx 0.24c$ using a 2-fold Leblanc density model Leblanc et al. 1998), while that of the type III burst in the same frequency range is about 10 kHz s^{-1} ($\approx 0.18c$). On the other hand, the faint envelope of type IIIb shows a very similar drift rate, of about 9 kHz s^{-1} ($\approx 0.16c$), to the drift rate of the regular type III burst. A similar speed difference between the exciters of type IIIb and the regular type III was found in previous studies (see e.g. Baselian et al. 1974; Baselyan et al. 1974; Sawant et al. 1978; Melnik et al. 2019) which suggests that the electron beams generating type IIIb were generally faster than those generating the regular type III bursts. It is important to note that such estimations of beam velocity from the spectral drift rate of type III radio bursts should only be used as first-order approximations since they assume a 1D radial density model (Jebaraj et al. 2020). Furthermore, the electrons generating type III radio emissions are discrete and should be considered as a distribution of energies are not mono-energetic (Mann et al. 2022).

The properties of stria substructures within the type IIIb burst observed at 06:44 UT (Fig. 5), are different in comparison to the stria bursts observed in the metric–decametric wavelength range. The duration of striae in this interplanetary type IIIb is 25% longer than the type III bursts (as reported by Melnik et al. 2019, in the decameter range). The bandwidth of the hecto–kilometric

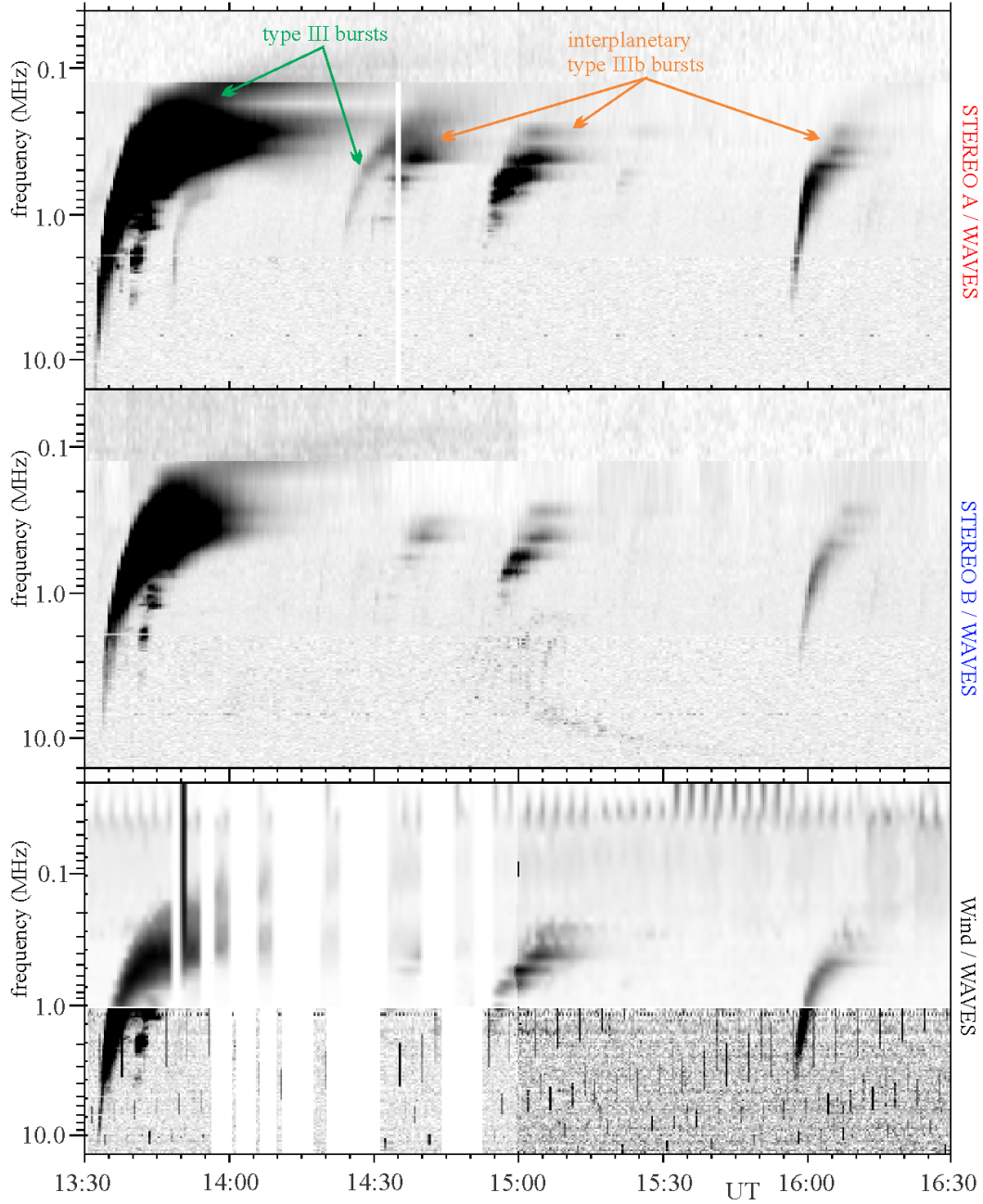


Fig. 2. Examples of a few structured interplanetary Type III bursts observed on 21 November 2011. The three type IIIb bursts show stria substructures, mostly visible in frequencies below 700 kHz. The type III burst with irregular substructure is visible at about 13:40 UT. This structured type III is possibly a harmonic component of the strong type III burst observed shortly after 13:30 UT.

stria elements presented here (about 70–120 kHz) is somewhat larger than those observed in the decameter wavelength range (about 60–80 kHz). We have found that the duration of striae can vary between 300 and 600 s, which is the typical duration of type III radio bursts in this frequency range.

Figure 4 shows that the radio bursts observed in the time interval 11:00–12:00 UT were most intense in the STEREO B observations. The stochastic appearance of type IIIb bursts, recorded in the radio event presented in Fig. 4 was also observed in the first radio event on 19 September 2011 (Fig. 3). The right panel of Fig. 4 shows the one-to-one schematic representations of the type III fine structures overplotted on the dynamic spectrum. The one-to-one schematic presentation of the fine structures was done on the STEREO B observations in which the

bursts were best observed. The identical schematic drawing was overlaid on STEREO A and Wind observations in order to compare the morphological characteristics of structured bursts, as observed by different spacecraft. We note that only a few of the most intense structures were observed by all three spacecraft. The different colours indicate fine structures belonging most probably to different radio bursts. We note that the perfect temporal coincidence of the type III fine structures, as observed by two different spacecraft, should be expected only in the case when the electron beam that generates type III burst propagates exactly in the middle between the two spacecraft. Otherwise, a shift in the time profile of the fine structures is observed (i.e. the signal is recorded earlier by the spacecraft toward which the electron beam is propagating). Additionally, the intensity of the

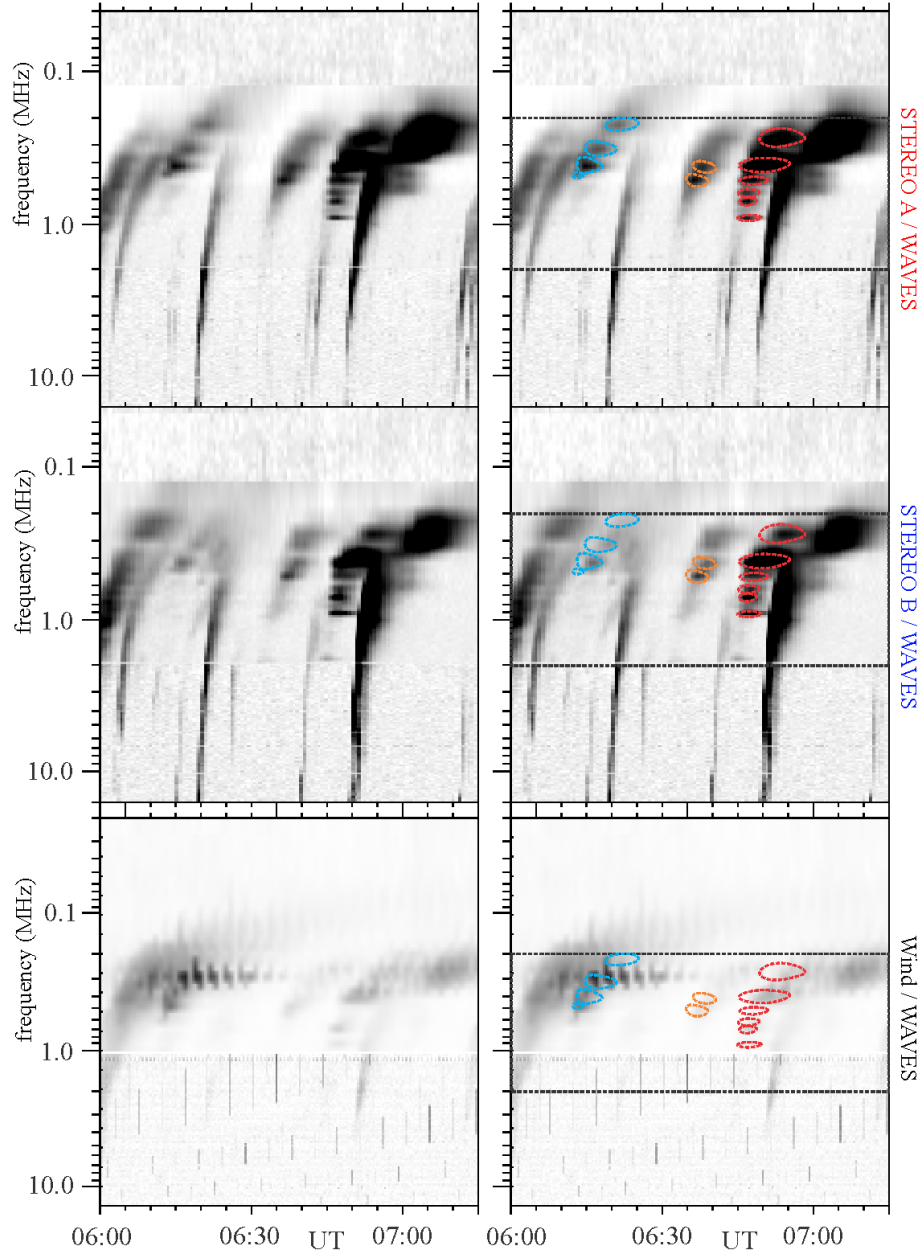


Fig. 3. Radio dynamic spectra observed on 19 September 2011 between 6:00 UT and 7:30 UT. (a) IP type IIIb bursts consisting of stria substructures observed along with multiple regular type III radio bursts by STEREO A & B. (b) Schematic representation of the stria substructures as observed by STEREO A and overlaid on STEREO B and Wind observations. The frequency range (2000–200 kHz) in which the IP type IIIb bursts were observed is indicated by the black frame.

radio emission increases or decreases depending on whether the electron beam propagates toward or away from the spacecraft that records the dynamic spectrum.

The stria substructures of two type IIIb bursts observed during two radio events on 19 September 2011 (Figs. 3 and 4) have many similarities. However, the organization of the stria substructures is more random in the second type IIIb, and the envelope of the burst is very faint. The stria substructures are clearly observed only by STEREO B, but the intensity of the radio emission seems to be greater in the Wind observations. These radio events seem to be associated with an eruption from the NOAA AR11302. We found a number of type IIIb bursts with similar stria-like substructures a few days earlier and later than 19 September 2011.

3.1.4. Time profiles for 19 September 2011 event

In this section we discuss the two subsequent type III bursts, the type IIIb burst with stria substructures and the regular type III burst that followed it. Figure 3 shows two bursts starting at about 06:44 UT and 06:50 UT. The bright stria substructures of type IIIb bursts are observed in the frequency range of 1000–200 kHz. The observed characteristics of the type III bursts enabled a qualitative interpretation of the dynamic properties of the substructures based on the properties of beam-plasma interaction in randomly inhomogeneous plasma (Krafft et al. 2013, 2014, 2015; Voshchepynets et al. 2015; Voshchepynets & Krasnoselskikh 2015; Krasnoselskikh et al. 2019).

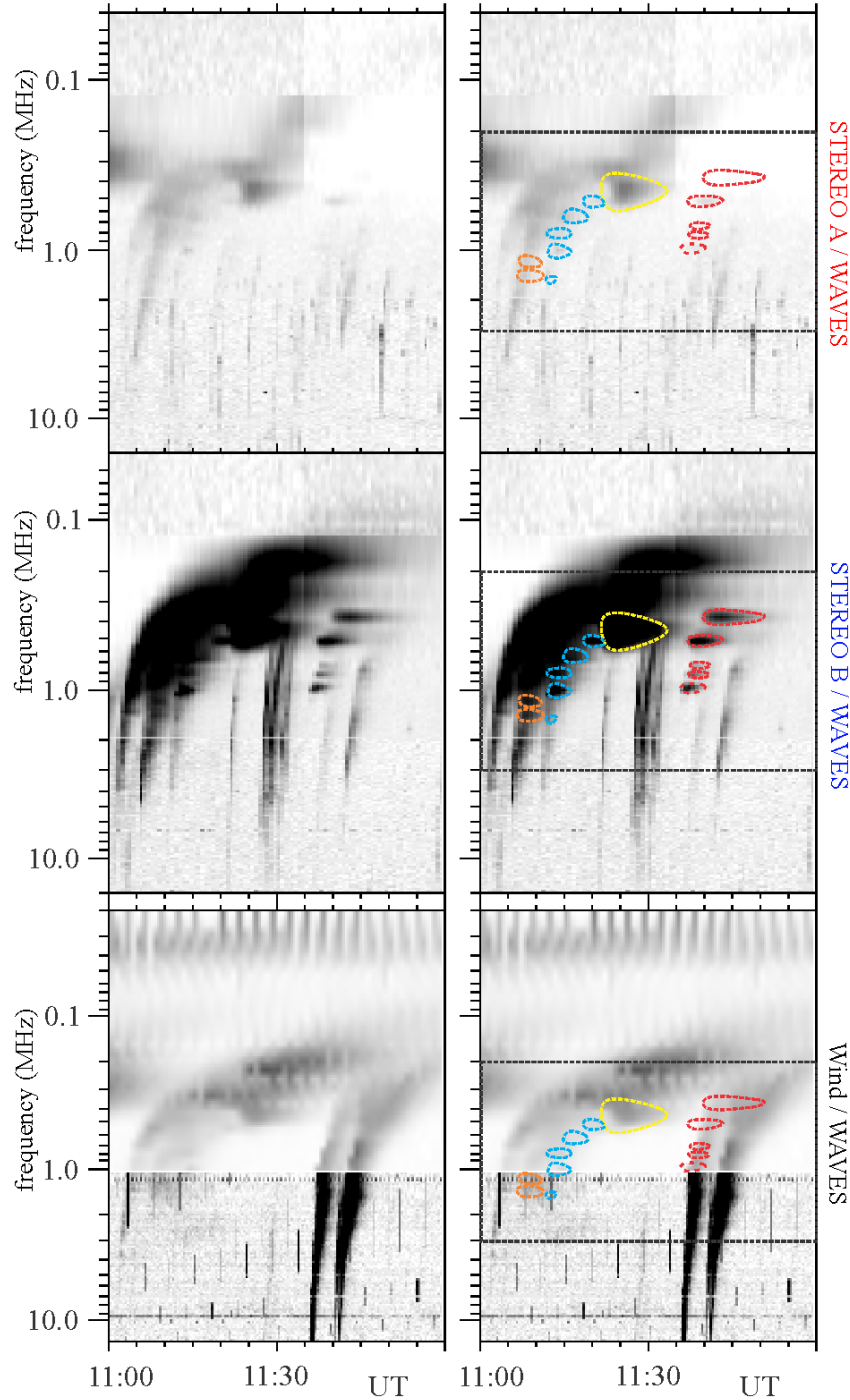


Fig. 4. Radio dynamic spectra observed on 19 September 2011 shows a group of type III bursts. (a) Type III bursts with stria substructures were observed along with regular type III radio bursts. Emission was strongest in observations by STEREO B. (b) Schematic representation of the outlines of the stria structures as observed by STEREO B and overlaid on STEREO A and Wind observations. The black frames in the *right panel* represents the same frequency range of 3000–200 KHz.

Figure 5a presents a detail of the radio dynamic spectra recorded on 19 September 2011 (Fig. 3). The colored arrows indicate the frequencies of the time profiles of the two observed bursts (Fig. 5 panels b and c). The dynamic spectrum clearly shows that the type IIIb burst consists of faint envelop emission and intense stria substructures. The time profiles at a few selected frequencies, crossing mostly through the central part of striae (labeled SE-a, b, c, d, and e), are presented in Fig. 5a. The time profiles of the envelope (Fig. 5c) have a noticeably lower

intensity that the time profiles of the striae, and the difference can be as large as one order of the magnitude.

Type III radio bursts often have a Gaussian rise profile and a power-law decay profile, with the rise time being significantly shorter than the decay time (e.g. Reid & Ratcliffe 2014); however, an exponential decay profile has also been recently reported by Krupar et al. (2018). This characteristic is also clearly visible in the profiles presented in Fig. 5. The peaks of the type III profiles show a systematic shift in time (higher to lower frequency),

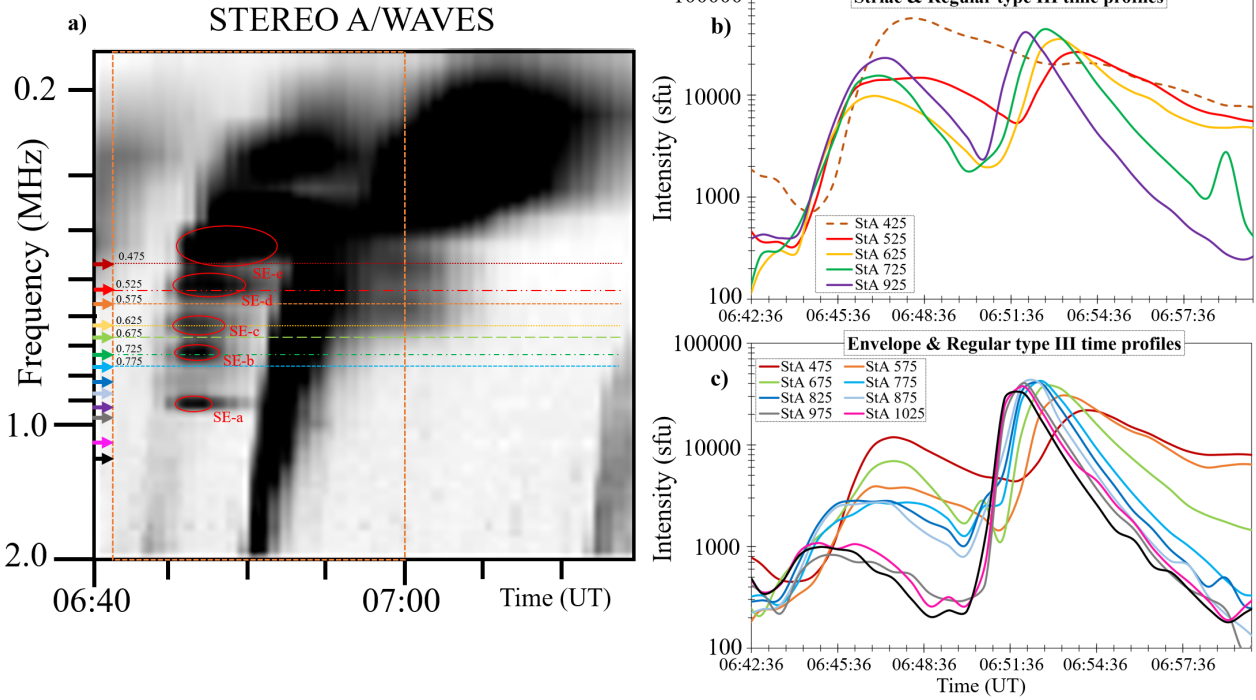


Fig. 5. Spectral analysis of the type III and type IIIb bursts observed on 19 September 2011. (a) Type IIIb bursts with stria substructures observed by the STEREO A spacecraft. The structured type III burst is followed by a relatively intense regular type III burst. (b) Intensity-time profiles of the type IIIb envelope and regular type III burst at selected frequencies. (c) Intensity-time profiles along the stria substructures and regular type III burst. The selected frequencies (at panels b and c) are indicated by the arrows of corresponding colors in panel a. The time interval plotted in panels (b) and (c) is within the orange box in panel (a).

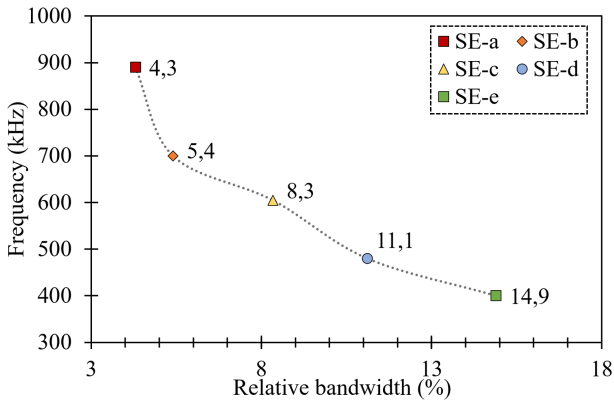


Fig. 6. Relative bandwidth of the different stria elements represented by the abbreviations SE-a through SE-e. The values are presented as percentages of the central observing frequency.

indicating the propagation of the electron beam and decrease in the ambient solar wind density. This characteristic may not be as clearly seen in the case of the stria substructures. However, we do observe an increase in relative bandwidth and stria duration with a decrease in observing frequency. Figure 6 shows the change in the relative bandwidth of the striae, presented as a percentage of the central frequency. This behavior results from the angular broadening of the electron beam (caused by diverging magnetic field lines), as the beam propagates away from the Sun and the region occupied by the beam at each instance increases. A consequence of the increasing area of the beam is that the macroscopic inhomogeneity of the solar wind density increases within the area covered by the beam.

Figure 7a shows the comparison of the characteristics of the striae and the envelope in the frequency range 450–800 kHz. Time profiles at 525 kHz, 625 kHz, and 725 kHz cross the central part of the striae, and the other profiles correspond to the envelope. The profiles show an exponential growth up to the maximum of the time profile and then a significantly slower decay. The growth rate of the time profile at 725 kHz, which is at the center of the stria element, is significantly higher than the growth rate for frequencies 775 kHz and 675 kHz which cross the envelope on the lower and higher frequency side of the striae. A similar behavior was found for the time profile of the stria element at 625 kHz, and the closest envelope profiles at 675 kHz and 575 kHz. The time profile at the 525 kHz, which is close to the central frequency of SE-d is somewhat different. Instead of a single maximum we observe a kind of plateau that might result from a combination of two Gaussian profiles similar to those at 725 and 625 kHz that follow one after another and overlap (dotted red curves in Fig. 7a). The neighboring 575 kHz profile that passes through the envelope has a significantly lower growth rate and a factor of four smaller amplitude. On the other hand, the time profile at 475 kHz passing through the lower frequency envelope shows a higher amplitude than the time profiles of other envelope regions; the envelope region through which the 475 kHz time profile is crossing is close to and partially includes some higher frequency parts of SE-e. A comparison of the maximum amplitude of these spectral lines show the very same ordering (Fig. 7b).

3.2. Type III bursts with triangular fine structures

3.2.1. General characteristics

Type III bursts with triangular fine structures are the second class of structured interplanetary type III bursts. This type of burst is

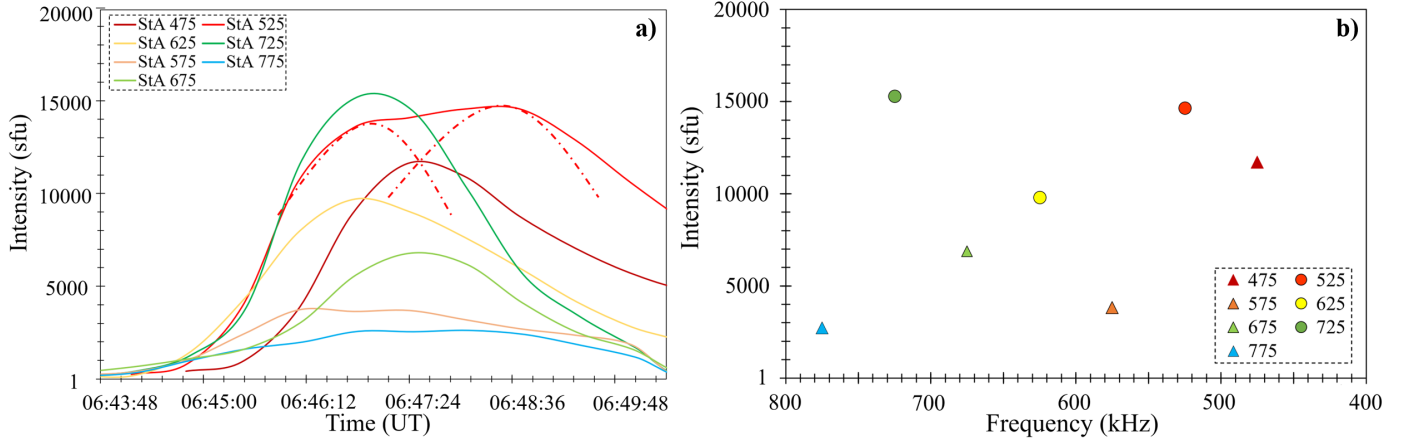


Fig. 7. Spectral characteristics of the striae and envelope in the frequency range 800–450 kHz. Panel (a) shows the time profiles of the SE and their envelope in the given frequency range. The red dotted Gaussian curves represent the two-peak morphology of the 525 kHz frequency band. Panel (b) shows the amplitude of the striae and envelope presented in panel (a). The triangles and circles represent the peak amplitude of the envelope and stria elements, respectively.

rarely observed, in comparison with the interplanetary type IIIb bursts. Figure 8 shows one group of these structured bursts. The spectral morphology of type III bursts with triangular fine structures is visibly different from the morphology of the type IIIb bursts presented in the previous section. The triangular substructures can be periodical, within the type III envelope, and they often partially overlap. Therefore, it is frequently difficult to distinguish between the fine structures and the underlying envelope. As can be seen in Figs. 8 and 9, the starting frequency of triangular substructures is generally higher than in the case of type IIIb bursts and even goes up to 5 MHz.

We find that the bandwidth of triangular substructures is generally between 90 and 120 kHz, which is larger than in the case of stria substructures. The full duration, estimated from the vertex to the base of the triangle (i.e. height of the triangle) at 5 MHz is about 60 s, and 300 s at 200 kHz. The occurrence of the triangular substructures within the type III envelope decreases with frequency. Furthermore, it seems that the triangular fine structures are composed of very narrowband stria substructures (Fig. 10), which are at the limit of the frequency and the time resolution of the WAVES observations.

3.2.2. Radio event on 12 November 2010

Figure 8 shows five different type III bursts observed by all three spacecraft on 12 November 2010. All type III bursts, except the one observed at about 08:25 UT, are structured. We observe a significant difference between the morphology and bandwidths of the triangular fine structures and the stria bursts, as discussed in the previous section.

The one-to-one schematic of the type III fine structure can be seen in Fig. 8b. The bursts are the most intense in STEREO B observations, and therefore we use it as a reference for the comparison of morphological characteristics with STEREO A and Wind. The comparison of observations by three different spacecraft shows a very good match between all the fine structures, confirming that they are not due to the receiver artifact, or to some technical problem.

We find the structured type III burst, observed at about 08:11 UT, very particular. The details of this radio burst are presented in Figs. 9 and 10. In addition to being observed by the WAVES instruments, this structured type III was also observed

by the Nançay Decametric Array (NDA; Boischoat et al. 1980) at higher frequencies. Other bursts in the group (Fig. 8) were either not in the time window of the NDA observations or (like the last burst in the group) were not observed. The NDA observations of structured type III burst suggest that the source of the radio burst was located on the visible side of the Sun, as seen from Earth. The fast electron beam generating this type III probably propagated mostly in the direction of STEREO B/WAVES, starting from the high latitudes with the trajectory allowing it to be observed by all three instruments.

3.2.3. Time profiles for the 12 November 2010 event

We performed the spectral analysis of the radio bursts as described in Sect. 3.1.4. The single frequency profiles of the triangular substructures of the type IIIb burst observed at 08:10 UT on 12 November 2010 are shown in Fig. 11. We selected observations from STEREO B/WAVES in which the intensity of this patchy burst is highest; see Fig. 9, panel (a).

For the analysis of the time profiles, we selected the triangular structure observed between 2 and 1 MHz, and the structure observed between 700 and 600 kHz. Figure 9a shows a zoomed-in image of the spectra, and the time profiles at frequencies that observe the bright triangular substructure (Fig. 9b). The envelope for this class of type III cannot be well distinguished due to overlapping fine structures.

The time profiles of the triangular substructures overlap in the rise phase of a burst, and their maximum is reached at similar flux values. At 1075 and 1125 kHz, the full time profiles of the burst are shifted about 5 s forward. The time profiles at frequencies above 1125 kHz have an approximately simultaneous rise time, and most of them show the presence of a double-peaked distribution of varying intensity, indicating possibly the presence of fundamental and harmonic components.

The time profiles of the triangular substructure observed at 725, 625, and 675 kHz (Fig. 9b), and the structures observed at higher frequencies have comparable intensities but the morphology of the profiles is different. The profiles at three low frequencies are flatter than those at frequencies above 1000 kHz, and their start time is shifted for about 10 s later. The flattening and the time shift of the profiles indicate the sudden decrease in the velocity of the electron beam responsible for generation of

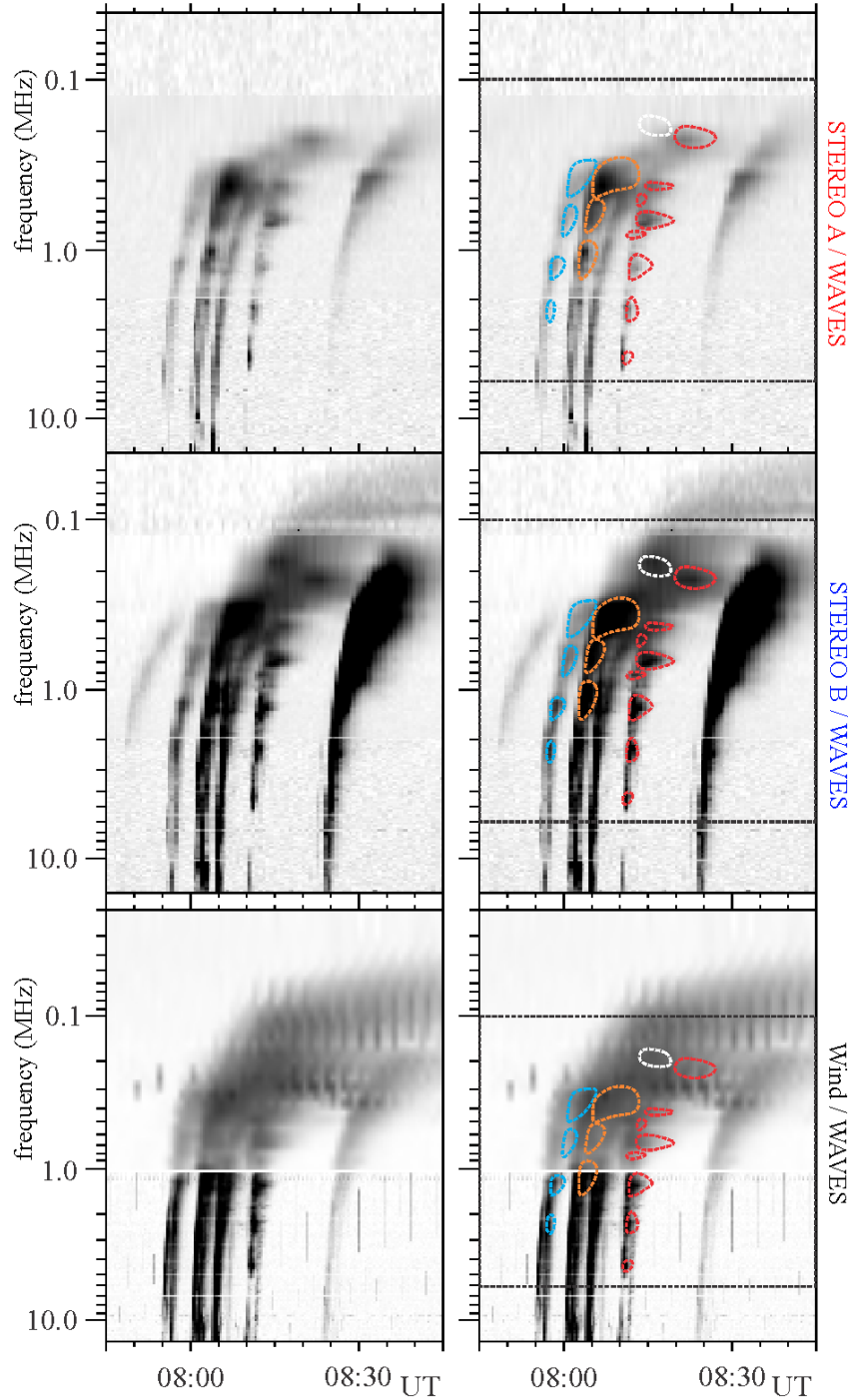


Fig. 8. Radio dynamic spectra observed on 12 November 2010. (a) Triangular stria substructures observed along with regular type III radio bursts by all three spacecraft (STEREO A & B, and Wind) at about 08:10 UT. (b) Schematic representation of the outlines of the triangular stria substructures as observed by STEREO B and overlaid on STEREO A and Wind observations. the spectrum also shows other regular type III radio bursts during the same time period.

the radio emission (see e.g. [Baselian et al. 1974](#); [Baselyan et al. 1974](#); [Sawant et al. 1978](#)) Generally, the drift rate of the structured type III is 13 kHz s^{-1} i.e. $\approx 0.23c$. This drift rate is comparable to that of the regular type III burst observed during the same radio event (about 10 kHz s^{-1} , i.e. $\approx 0.18c$).

In order to investigate the complex maxima of the time profiles presented in Fig. 9 we also examine the Wind/WAVES RAD 2 observations in the frequency range 10–1 MHz. These observations have better spectral resolution (50 kHz and 200 kHz, respectively) and comparable temporal

resolution to the STEREO/WAVES HFR2 spectra (20 s and 16 s, respectively). While STEREO observations show one structured type III burst at about 08:11 UT (Fig. 9), the Wind observations show two structured bursts, at 08:10:30 UT and 08:12:00 UT (Fig. 10a). It is possible that these two bursts are the fundamental and harmonic component, but from the available observations this is not clear. Both bursts are composed of a number of striae of varying intensity, and it seems that the dense and intense striae compose the broadband triangular structures of the type III bursts (Fig. 10). The stria substructures are similar to

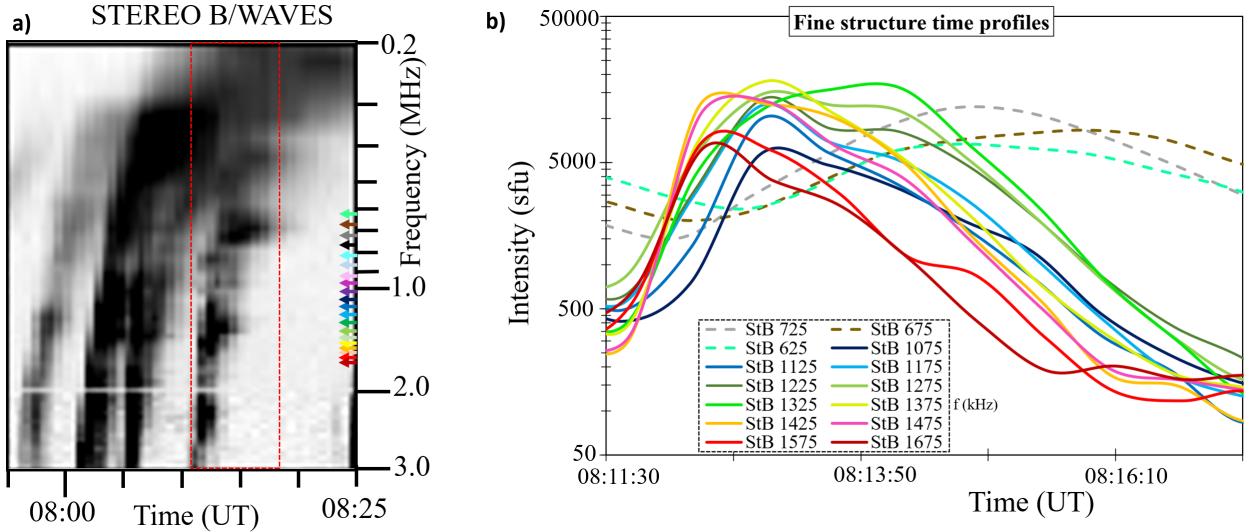


Fig. 9. Spectral analysis of the structured type III burst observed on 12 November 2010. (a) Type III burst with triangular fine structures, observed at about 08:11 UT by the STEREO B spacecraft. The considered frequency range is from 14 to 1 MHz. The dotted red box represents the range where the time profile analysis was performed. The colored arrows in the Y-axis represent the frequencies at which the time-profiles in panel (b) were made. (b) Time profiles of triangular substructures. The colors represent the same frequencies as in panel (a).

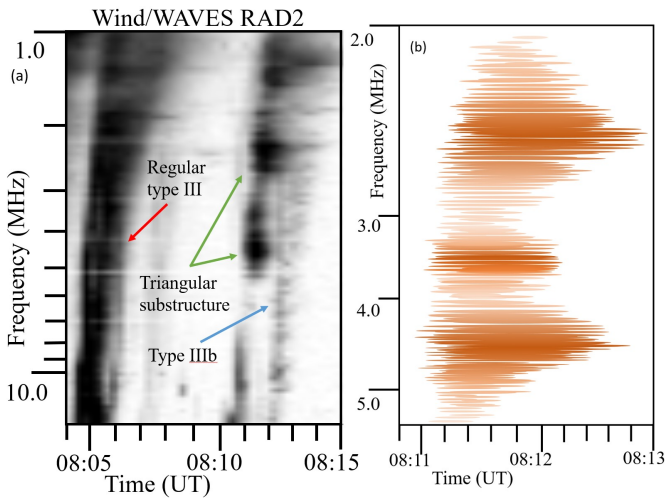


Fig. 10. Fine structures within the triangular stria substructure. (a) Group of type III burst in the frequency range 14 to 1 MHz, observed by the Wind/WAVES RAD 2 instrument. The red arrow points to the regular type III burst observed at around 08:05 UT. The blue arrows point to the two structured type III bursts, while the green arrow indicates the periodic substructures observed at 08:11 UT. (b) Sketch of the structured type III burst observed at 08:11:00 UT and 08:13:00 UT.

those found composing the type IIIb bursts (Sect. 3.1.3). The striae have bandwidths of approximately 30–80 kHz; the lowest measured bandwidth is in the limit of the resolution of the Wind/WAVES RAD 2 observations. These observations indicate that striae of lower bandwidth may also exist, but they are not resolved. The duration of the striae is about 30 s when presumably they do not form the triangular substructure, and 60 s when within the triangular structure. We note that the decay time of type III bursts in this frequency range is about 60 s.

3.3. Type III bursts with irregular substructures

The last class of structured interplanetary type III bursts are those with irregular fine structures. Figure 11 shows a few examples

of type III bursts with irregular substructures. As we can see, type III bursts in this class have fine structures that do not show a periodicity or regularity in their morphology. They are more seldom observed than other types of structured type III bursts, and their fine structures can strongly vary in bandwidth, duration and shape (Fig. 11). The morphology of the envelope of type III radio bursts with irregular substructures is similar to the ordinary type III radio bursts. It was not possible to analyze these bursts in a systematic way, and individual case studies are necessary to possibly draw some more general conclusions.

Figure 11a shows an example of type III radio burst with irregular fine structures as observed by STEREO A/WAVES on 30 November 2011. The intensity of the type III burst slowly decreases from about 10 MHz to 2 MHz. Starting from about 1200 kHz, emission is well observed again, composed of dot-like fine structures within the type III envelope. The bandwidth of the dot-like fine structures is narrow ($\ll 40$ –60 kHz), and the duration seems to be significantly shorter than for the type III bursts at these frequencies. However, the structures are on the edge of the time–frequency resolution and it is not possible to reliably estimate their duration and bandwidth. The structured type III is subsequently followed by a faint and fuzzy type III burst without clearly distinguishable fine structures. These two bursts could be the fundamental and harmonic components of the same burst. A similar fundamental-harmonic pair was recently reported in the decameter wavelength range (Zhang et al. 2020).

Another group of type III radio bursts with irregular fine structures is presented in Fig. 11b. This very particular radio event, observed on 12 November 2010 (from about 13:30 until 15:50 UT) was associated with a flare–CME event. Eruptive events often strongly disturb the ambient plasma conditions and can produce turbulence in the plasma environment through which the electron beams propagate. This can result in a large number of fine structures observed in the associated radio emission (e.g. Magdalenic et al. 2020). The presented radio event also shows strongly fragmented radio emission. The event started at about 13:35 UT, with groups of highly structured type IIIb bursts observed by the Wind/WAVES RAD 2

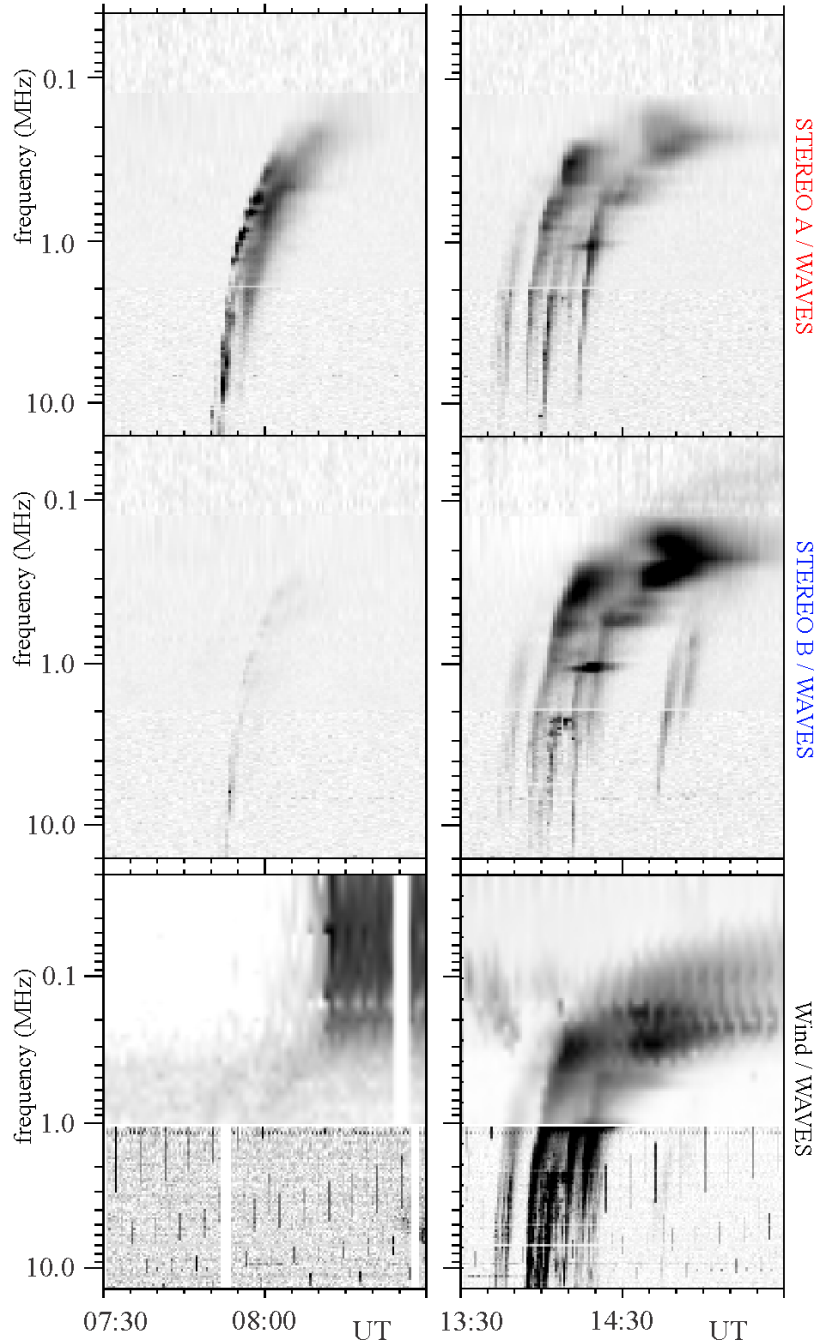


Fig. 11. Third class of interplanetary type III fine structures. (a) Radio dynamic spectra observed on 30 November 2011 between 7:30 UT and 8:30 UT, including an irregular type III burst with fine structures at 07:52 UT by the STEREO A and STEREO B spacecraft. (b) Radio dynamic spectra observed on 12 November 2010, including stria-like fine structures within the type III bursts observed at 13:45 UT, and large heart-shaped substructure and stria substructure in the STEREO/WAVES observations.

receiver (13–1 MHz). These bursts were very weak in both STEREO/WAVES observations. At about 13:45 UT, a new group of structured type III bursts were observed with irregular substructures and this time, better observed in STEREO/WAVES observations (Fig. 11). The fine structures in type III bursts associated with this event were not isolated in Wind/WAVES observations due to the overall higher intensity of the apparently overlapping radio bursts. The fine structures however, can be seen in STEREO A & B/WAVES where the emission intensity is not as high as that observed by Wind/WAVES. Very particular fine structures are observed in STEREO/WAVES observations

resembling large stria substructures, and even heart-shaped substructure (Fig. 11). The bandwidth of stria-like fine structures is ~ 100 kHz and their duration seem to increase with frequency decrease. The fine structures do not show any form of drift rate. These fine structures could be generated by the interaction between the electron beam and over-dense structures such as blobs in solar wind which are common in slow-solar wind (Sanchez-Diaz et al. 2017). Another possible interpretation could be that the fine structures are enhancements at discrete frequencies of a regular type III burst source (electron beam) that propagates in a highly turbulent medium.

4. A model for stria emission

It is difficult to explain all the different variations of the type III fine structures presented in this study. Therefore, we focus on the basic ideas that can explain the general features of structured bursts with stria elements. We do this by employing a detailed analysis of the radio event described in Sect. 3.1.3. The generation and time evolution of the stria elements within type III radio bursts can be self-consistently described using a probabilistic model (PM) of the beam-plasma interaction (BPI) in randomly inhomogeneous plasma (Krafft et al. 2013, 2014, 2015; Krafft & Volokitin 2016, 2017; Voshchepynets et al. 2015; Voshchepynets & Krasnoselskikh 2015; Krasnoselskikh et al. 2019; Tkachenko et al. 2021). Here we present a scenario for the generation of stria elements described in Sect. 3.1.3. We note that the same generation mechanism can be applied for the other type III fine structures presented in this study as well.

It is widely accepted that the generation of type III bursts is a two-step process (see for e.g. Ginzburg & Zhelezniakov 1958; Suzuki & Dulk 1985; McLean & Labrum 1985). Initially, the beam of fast electrons generates Langmuir waves which are then emitted in the form of electromagnetic waves. Therefore, the characteristics of the electromagnetic emission are determined by the characteristics of the electron beam and, by the processes of evolution of Langmuir wave spectra followed by radio emission. Since electrons are magnetized and move along the magnetic field lines, the increasingly larger emitting area corresponds to the diverging magnetic field lines. The emitting volume covers a large region that can be characterized by a rather wide range of plasma densities. Here we propose that the density fluctuations determine the characteristics of the type III fine structures (i.e. stria elements, their variations in brightness, dynamics, and in particular the duration of the growth phase).

The density fluctuations are ubiquitous in the heliosphere and can be present in a wide range of scales (Neugebauer 1975; Celnikier et al. 1983, 1987). We note that $\Delta n/n_0$ (average density fluctuations) changes based on length scales, and it may be in a very broad range. Considering 400 km gives a range 0.1–1% or less, but $\Delta n/n_0$ over larger distance (e.g. 40 000 km) could be 10% or more. We note that the correlation scales of density fluctuations can be determined only from direct in-situ measurement. These kinds of studies are rare (see e.g. Chen et al. 2020). The amplitude of the density fluctuations are not very large but are still important for the evolution of BPI. For this analysis we are particularly interested in fluctuations in the range of spatial scales between several hundred to several thousand times the wavelength of the Langmuir waves, up to the distances corresponding to the relaxation length of the beam in homogeneous plasma for each given frequency of wave. The relaxation length of the beam is defined as

$$L \sim \frac{\ln \Lambda V_b}{\gamma}. \quad (1)$$

Here V_b is the characteristic beam velocity, γ is the characteristic increment of BPI, and $\ln \Lambda$ is the Coulomb logarithm determined by the macroscopic parameters of plasma ($\Lambda \sim (n\lambda_D^3)$, n is the density, and λ_D is the Debye length).

Krasnoselskikh et al. (2019) show that the reflection of the Langmuir waves from the density inhomogeneities, even as low as 1%, can lead to a partial transformation of the energy of Langmuir waves into electromagnetic waves (i.e. radio emission). Recent observations show that the density fluctuations can be of small to moderate size, and they are usually in the range of 2–3%. However, density fluctuations as large as 7% (see for

e.g. Krupar et al. 2020) at distances corresponding to hectometer wavelength, are also reported. The bandwidths of stria structures reported in our study correspond to the low levels of density fluctuations, in agreement with Krasnoselskikh et al. (2019). The upper level of density fluctuations reported by Krupar et al. (2020) would result in a significantly large bandwidths of the stria elements.

The PM predicts two regimes of evolution of the Langmuir wave spectrum. In the first regime a level of the density fluctuations is low, the wave dispersion dominates and this results in the continuous growth of the Langmuir waves, which is not observed in the case of type III radio bursts. The condition for this regime can be given by

$$3k^2\lambda_D^2 > (<\Delta n^2/n_0^2>)^{1/2}, \quad (2)$$

where $<\dots>$ denotes averaged values. The second regime is characterized by a two-phase evolution of Langmuir waves (i.e. the initial growth is followed by the decay). The condition for the second regime is opposite to the previous regime and is defined as

$$3k^2\lambda_D^2 < (<\Delta n^2/n_0^2>)^{1/2}. \quad (3)$$

The generation of type III radio bursts occurs under conditions corresponding to the second regime when the Langmuir waves are generated by the beam with the phase velocity approximately equal to the beam velocity. In this case, when the beam propagates with a rather small angle to the background magnetic field, the dispersion term may be written as $k^2\lambda_D^2 \simeq T_e/W_b$ (where T_e is the temperature of the background plasma, and W_b is the characteristic energy of the beam).

In the case of beam energies of a few keVs to tens of keVs (the overwhelming majority of the bursts), the interaction takes place in the second regime where we assume $k^2\lambda_D^2 \simeq T_e/W_b$. The two different regimes of BPI are realized as a function of the ratio of two parameters: T_e/W_b and $(<\Delta n^2/n_0^2>)^{1/2}$ in the range of the characteristic scales determined above. Figure 12a shows the spectrum evolution when the density fluctuations are large enough to be dominant over the wave dispersion ($3T_e/W_b < (<\Delta n^2/n_0^2>)^{1/2}$).

A high level of density fluctuations also determines the process of electromagnetic wave generation at the fundamental plasma frequency (ω_{pe}). Specifically, when the density fluctuations dominate over the wave dispersion effects, the dominant process is the direct transformation of a part of Langmuir wave energy into electromagnetic waves. This happens in the vicinity of the density humps where the reflection of the Langmuir waves occur (Krasnoselskikh et al. 2019). This process also affects the evolution of the electromagnetic wave intensity, at the place of its generation. The intensity of electromagnetic emission evolves similarly to the evolution of Langmuir wave intensity. In the region where the Langmuir waves are generated, the growth phase of the electromagnetic emission is approximately the same as the growth phase of the Langmuir waves and depends on the level of the density fluctuations as shown in Fig. 12.

The numerical solutions presented in Fig. 12a were obtained under the conditions $n_b/n_0 = 10^{-5}$, $V_b = 16V_T$ (here we considered the thermal speed of electrons in the solar wind to be, $V_T = 0.01c$; Halekas et al. 2020), and for six different levels of average density fluctuations $<\Delta n/n_0>$ (adapted from Tkachenko et al. 2021). The increase in the level of density fluctuations induces at the same time an increase in the growth time of the wave and a decrease in the peak value of the wave amplitude.

Figure 12b shows that for electron beams of different velocity, the time needed for the growth of Langmuir wave energy,

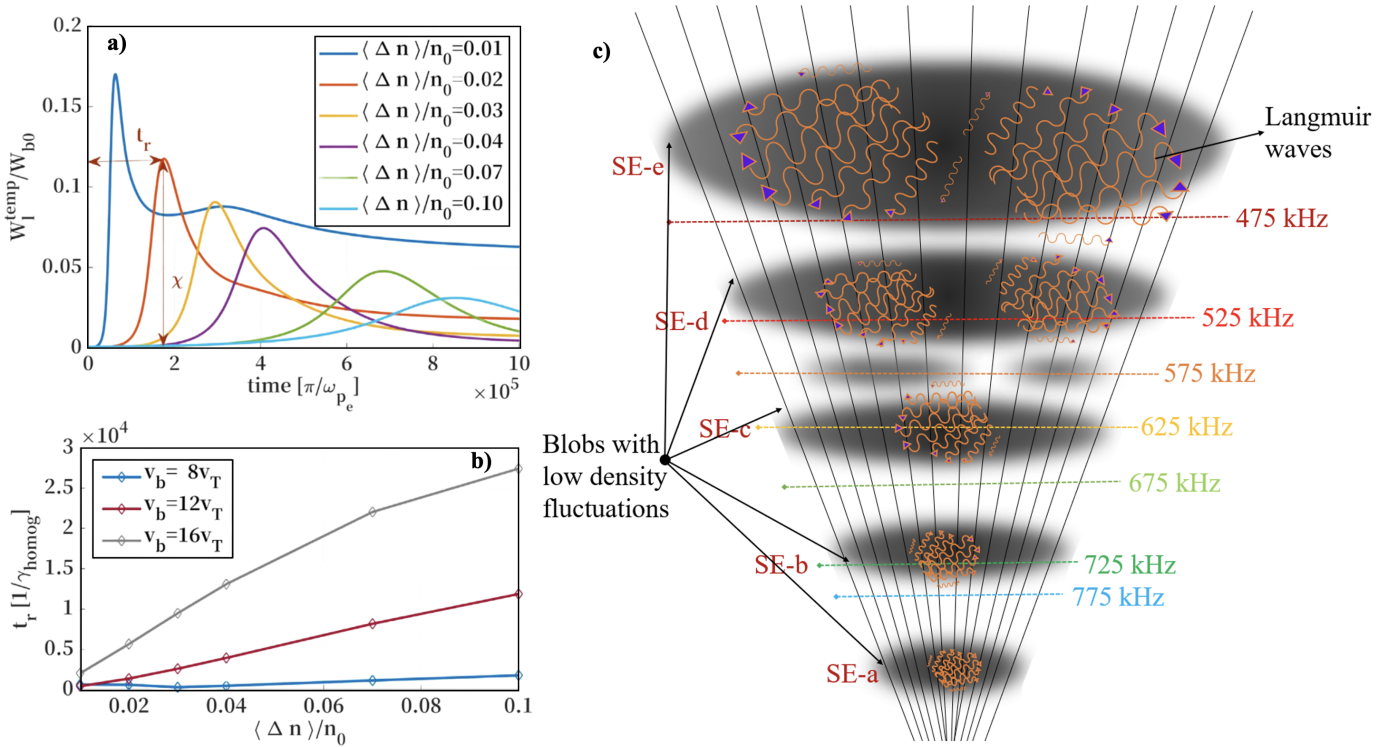


Fig. 12. Effects of random density fluctuations on the growth of Langmuir waves that lead to electromagnetic emission. (a) Temporal evolution of the Langmuir wave intensity W_L^{temp} , in units of electron beam energy W_b , is shown as a function of density fluctuation level. The time of growth of the Langmuir wave until the maximum amplitude x is denoted as t_r . (b) The time of growth of Langmuir wave energy (t_r , panel a) during the beam relaxation, in units of inverse growth rate for homogeneous plasma $t_r[1/\gamma_{\text{homog}}]$, is presented as a function of density fluctuations $\Delta n/n_0$. Three different electron beam speeds (V_b in units of the thermal speed V_T ; where V_T is $0.01c$) are considered. (c) Cartoon representation of an electron beam propagating through diverging magnetic field lines interacting with density blobs of different scales at different frequencies. The frequency levels are marked based on Fig. 5 and they roughly correspond to the different regions where the striae and envelope are observed. The enhanced growth of Langmuir waves is shown in different blobs with the wavy orange markers. Panels (a) and (b) were adapted from Tkachenko et al. (2021).

during the beam's relaxation, is greatly affected by the level of background density fluctuations. The faster beams need more time to relax when the levels of density fluctuations increases. These effects appear as a natural consequence when the electron beam propagates through regions of varying density. Figure 12c shows a sketch of regions with varying levels of density fluctuations and intensity of radio emission. The shaded areas represent increasingly larger blob regions where the level of density fluctuations is low in comparison to the ambient regions beyond the blob regions. In these areas the wave growth rate is high, the amplitude of the Langmuir waves is large, and accordingly the intensity of radio emission is also stronger. On the other hand, the nearby “envelope areas” correspond to higher levels of density fluctuations, smaller amplitudes of Langmuir waves, and consequently low intensity of radio emission. These regions correspond to the low intensity radio emission (i.e. the envelope of type IIIb).

We note that the times characterizing BPI are not exactly the same as the characteristic times of evolution of the observed radio spectrum. Specifically, depending on the characteristics of the ambient plasma, the radio emission can undergo different processes when propagating from the region where it was generated toward the observer.

When the plasma region where the radio emission is generated is optically thin, the electromagnetic waves propagate toward the observer with a small delay which is defined by the propagation time of light. When the source region of radio emission is optically thick, the initial stage of the growth phase of

the wave intensity profile will be similar to the growth of the Langmuir waves. The reason for that is the rather fast transformation of the Langmuir waves into electromagnetic waves in the case of fundamental radio emission. The duration of the decay phase can be determined by different processes such as electromagnetic wave diffusion on the same density fluctuations (e.g. Arzner & Magun 1999; Kontar et al. 2019, and references therein). In this case the decay phase of emission is determined by the characteristic time of electromagnetic wave diffusion in the regions close to the source region of the radio emission. This characteristic time may therefore increase with increasing levels of background density fluctuations.

Figure 13 shows the rise times for the striae and envelope time profiles (see Fig. 7a). The characteristic time of the rising phase of the burst t_r (Fig. 12b) can be estimated as

$$t_r \sim \alpha/\gamma_{\text{lh}}. \quad (4)$$

In this relation, α is the coefficient characterizing the dependence of the growth phase for different levels of density fluctuations (as presented in Fig. 12a) and γ_{lh} is a linear increment of BPI in homogeneous plasma that is defined as

$$\gamma_{\text{lh}} \simeq \omega_{pe} \frac{n_b}{n_0} \left(\frac{V_b}{\Delta V_b} \right)^2. \quad (5)$$

In order to evaluate Eq. (5) for the striae observed in Fig. 5, the characteristic rise times of the stria elements

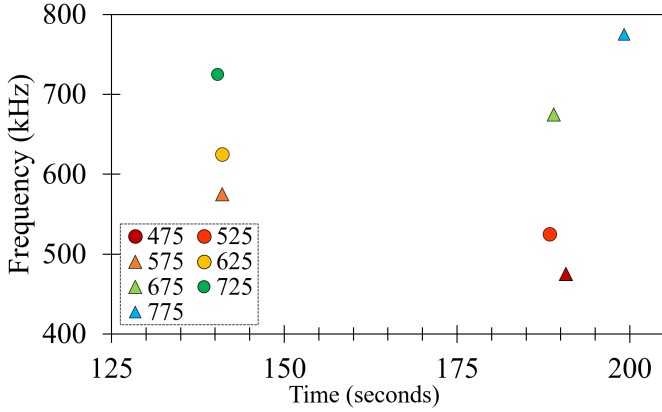


Fig. 13. Rise times of the frequency–time profiles corresponding to the striae and their envelope in the frequency range of 800–400 kHz. The triangles and circles represent the rise times of the envelope and stria elements, respectively.

can be calculated assuming the following: $(V_b/\Delta V_b) \approx 10$, $n_b/n_o \approx 10^{-7}–10^{-6}$, and $\omega_{pe} \approx 2\pi \cdot 7 \times 10^{-5}$. We obtain $\gamma_{lh} \approx 0.5 \times 10^2$ s and this characteristic time corresponds to the typical parameters of the usually observed energetic electron fluxes, and is also in agreement with the estimates presented in Fig. 13.

5. Discussion and conclusions

Fine structures of solar type III radio bursts can provide information about the ambient plasma conditions, such as coronal density and the magnetic field (Dulk & McLean 1978). To date the majority of studies of radio fine structures have been performed at metric–decametric wavelengths (see e.g. Chernov 2011). Recently, the new state-of-the-art instruments such as the LOw Frequency ARray (LOFAR van Haarlem et al. 2013) provide us with high time and frequency resolution, and high sensitivity observations that bring completely new insights into the particle acceleration and propagation processes (see e.g. Magdalenic et al. 2020).

Studies of fine structures observed in the hectometer and kilometer wavelengths are very rare, even in the STEREO era, during which multi-point observations of the Sun are available. This work reports for the first time on the structured type III radio bursts from space-based observations. We used observations of all three WAVES instruments to confirm that the observed fine structures are not due to the instrumental artifacts. It was not possible to use the radio triangulation technique due to the unfavorable spacecraft separation (around 180 degrees).

Based on their morphological characteristics, we can distinguish three main classes of structured interplanetary type III bursts: (a) interplanetary type IIIb bursts, (b) type III with triangular substructures, and (c) type III bursts with irregular fine structures. The morphological similarities between metric–decametric and interplanetary type IIIb bursts indicate that the generation mechanism of the interplanetary type IIIb bursts could be inherently similar to that of the metric and decametric type IIIb bursts (Li et al. 2012; Reid & Kontar 2021). The elementary substructures of type IIIb bursts, in both frequency ranges, are called striae. We compared the type III fine structures observed by three different spacecraft, and using one-to-one schematic presentation of the fine structures. This comparison allowed us to confirm that the type III fine structures are not due to instrumental effects.

Below we list some important results of the study.

- The time profiles of type IIIb bursts and their fine structures show that the stria substructures have much higher intensity than the type IIIb envelope. The profiles of type IIIb burst are also more symmetrical than the profiles of the regular type III bursts. The envelope emission has a nearly symmetrical Gaussian profile which is significantly different from the exponentially-modified Gaussian profiles of regular type III radio bursts. The stria time profiles on the other hand are asymmetric, but not to the level of the regular type III bursts.
- The Wind/WAVES RAD 2 observations show that triangular substructures of type III bursts are possibly composed of a number of very narrowband stria substructures (Fig. 10). This is probably the reason why the triangular substructures show complex morphology and time profiles.
- The general characteristics of type III substructures are listed in Table 1. We also found that the lower limit of the stria bandwidth seem to be imposed by the frequency resolution of the observations and that the intensity enhancements observed within type III bursts are sometimes clearly composed of a number of stria substructures (Fig. 10).

Numerous studies reported type III fine structures in the metric–decametric wavelengths (see e.g. de La Noë et al. 1976; Melnik et al. 2019, 2021; Kontar et al. 2017; Chen et al. 2018; Sharykin et al. 2018). Some of these studies also discuss the possibility that the structured type III bursts are precursor of the regular type III bursts, and that the stria bursts in the decametric type III–IIIb pair become more densely spaced toward the low frequency part of the bursts. This may be the reason why the stria bursts in the hectometer wavelengths appear to become quasi-continuous and are not well resolved in the presently available observations.

Recently Pulupa et al. (2020) and Chen et al. (2021) presented observations of a hectometric type IIIb radio burst recorded by the Parker solar probe (PSP; Fox et al. 2016). The clear individual stria bursts were observed close to 1 MHz, but not below that frequency. To our knowledge, all the studies to date have only addressed observations of structured type III bursts in the metric to the low decametric wavelengths. This study presents structured type III bursts in the hecto-kilometric wavelengths (interplanetary type IIIIs) for the first time, and presents open questions about the generation mechanism of the observed structuring in the temporally and spatially varying interplanetary plasma.

We note that such well-defined fine structures like the ones presented in this work are rarely observed. We performed a survey of the interplanetary radio observations, taken by STEREO A, STEREO B, and Wind, considering a two-month period (01 September 2011–01 November 2011). We found a total of about 710 type III radio bursts, of which ~45% (310 bursts) were observed by all three spacecraft. Type III bursts with fine structures make up about 16% of the total type III bursts (118 bursts), of which 41 bursts were observed by all three spacecraft. The majority of structured type III bursts in the considered time interval were observed by one or two spacecraft. Furthermore, we found 15 cases (about 2%) of type III bursts with very well-defined fine structures (belonging to the first and second categories defined in this study). On the other hand, irregular substructures (the third category) were found far more frequently and accounted for the remaining 103 bursts.

We proposed an explanation for the generation of stria bursts employing the probabilistic model and simulations for the beam–plasma interactions (Krafft et al. 2013, 2014, 2015; Krafft & Volokitin 2016, 2017; Voshchepnyets et al. 2015;

Voshchepynets & Krasnoselskikh 2015; Krasnoselskikh et al. 2019). This widely discussed model can explain the generation of structured radio emission, regardless of the observing frequency range, assuming that the variations in the level of density fluctuations at different distances from the Sun result in variations of the average level of the wave amplitudes of the Langmuir waves. This in turn results in different level of the electromagnetic emission. This phenomenon is taken into account in the PM of BPI and its effects on the different rise and decay phases of the evolution of BPI (Krafft et al. 2013). As a result, some of the source regions of the radio emission are associated with high intensities and some with low intensities of radio emission. Observations confirming such a scenario are presented in Sect. 4.

If the stria bursts are generated due to the density inhomogeneities in the corona, they will also be dependent on the scale length of these density inhomogeneities, and on other plasma parameters such as the ion and electron temperature (Ledenev et al. 2004; Li et al. 2012). Since the scales of density fluctuations in the interplanetary space are much larger than in the low corona (see e.g. Spangler 2002; Krupar et al. 2020), we can expect that the morphology of the striae in the interplanetary space will also reflect this difference. The observations presented here indeed show that the interplanetary type IIIb bursts have stria substructures with somewhat larger bandwidths than those observed in the metric-decametric wavelength range.

However, in order to be able to perform a more in-depth study of the type III fine structures, we need high resolution observations, preferably from two different points of view so the 3D location of the sources or radio emission can be estimated employing radio triangulation (e.g. Magdalenic et al. 2014; Jebaraj et al. 2020). This additional information on the source positions of the radio emission will allow us to understand the type of ambient coronal structures through which the fast electron beams propagate. The observations from the novel missions, such as the Parker Solar Probe (PSP) and the Solar Orbiter (SolO; Müller & Marsden 2013) can help us understand the nature of the fragmented radio emission and their generation mechanism.

Acknowledgements. The STEREO/SECCHI data are produced by a consortium of RAL (UK), NRL (USA), LMSAL (USA), GSFC (USA), MPS (Germany), CSL (Belgium), IOTA (France), and IAS (France). The Wind/WAVES instrument was designed and built as a joint effort of the Paris-Meudon Observatory, the University of Minnesota, and the Goddard Space Flight Center, and the data are available at the instrument Website. We thank the radio monitoring service at LESIA (Observatoire de Paris) for providing value-added data that have been used for this study. I.C.J. was supported by a PhD grant awarded by the Royal Observatory of Belgium. I.C.J. and J.M. acknowledge funding by the BRAIN-be (Belgian Research Action through Interdisciplinary Networks) project CCSOM (Constraining CMEs and Shocks by Observations and Modelling throughout the inner heliosphere), and BRAIN-be project SWiM (Solar Wind Modeling with EUHFORIA for the new heliospheric missions). V.K. (Vratislav Krupar) was supported by NASA grants 18-2HSWO2182-0010 and 19-HSR-192-0143. S.P. has received funding from the European Union's Horizon 2020 research and innovation programme under grant agreement No 870405, and the projects C14/19/089 (C1 project Internal Funds KU Leuven), G.0D07.19N (FWO-Vlaanderen), SIDC Data Exploitation (ESA Prodex-12).

References

Arzner, K., & Magun, A. 1999, *A&A*, **351**, 1165
 Baselian, L. L., Goncharov, N. I., Zaitsev, V. V., et al. 1974, *Sol. Phys.*, **39**, 213
 Baselyan, L. L., Goncharov, N. Yu., Zaitsev, V. V., et al. 1974, *Sol. Phys.*, **39**, 223
 Bhonsle, R. V., Sawant, H. S., & Degaonkar, S. S. 1979, *Space Sci. Rev.*, **24**, 259
 Boischot, A., Rosolen, C., Aubier, M. G., et al. 1980, *Icarus*, **43**, 399
 Bougeret, J.-L., Kaiser, M. L., Kellogg, P. J., et al. 1995, *Space Sci. Rev.*, **71**, 231
 Bougeret, J.-L., Goetz, K., Kaiser, M. L., et al. 2008, *Space Sci. Rev.*, **136**, 487
 Celnikier, L. M., Harvey, C. C., Jegou, R., Moricet, P., & Kemp, M. 1983, *A&A*, **126**, 293

Celnikier, L. M., Muschietti, L., & Goldman, M. V. 1987, *A&A*, **181**, 138
 Chen, C. H. K., Bale, S. D., Bonnell, J. W., et al. 2020, *ApJS*, **246**, 53
 Chen, L., Ma, B., Wu, D., et al. 2021, *ApJ*, **915**, L22
 Chen, X., Kontar, E. P., Yu, S., et al. 2018, *ApJ*, **856**, 73
 Chernov, G. P. 2011, *Fine Structure of Solar Radio Bursts* (Springer), 375
 Chernov, G. P., Stanislavsky, A. A., Konvalenko, A. A., et al. 2007, *Astron. Lett.*, **33**, 192
 de La Noe, J., & Boischot, A. 1972, *A&A*, **20**, 55
 de La Noë, J., Møller-Pedersen, B., & Boischot, A. 1976, *Sol. Phys.*, **46**, 505
 Dulk, G. A., & McLean, D. J. 1978, *Sol. Phys.*, **57**, 279
 Ellis, G. R. A., & McCulloch, P. M. 1967, *Aust. J. Phys.*, **20**, 583
 Erickson, W. C. 1997, *PASA*, **14**, 278
 Fox, N. J., Velli, M. C., Bale, S. D., et al. 2016, *Space Sci. Rev.*, **204**, 7
 Ginzburg, V. L., & Zhelezniakov, V. V. 1958, *Sov. Astron.*, **2**, 653
 Halekas, J. S., Whittlesey, P., Larson, D. E., et al. 2020, *ApJS*, **246**, 22
 Howard, R. A., Moses, J. D., Vourlidas, A., et al. 2008, *Space Sci. Rev.*, **136**, 67
 Jebaraj, I. C., Magdalenic, J., Podladchikova, T., et al. 2020, *A&A*, **639**, A56
 Jebaraj, I. C., Kouloumvakos, A., Magdalenic, J., et al. 2021, *A&A*, **654**, A64
 Kaiser, M. L. 2005, *Adv. Space Res.*, **36**, 1483
 Kellogg, P. J. 1980, *ApJ*, **236**, 696
 Kontar, E. P., Yu, S., Kuznetsov, A. A., et al. 2017, *Nat. Commun.*, **8**, 1515
 Kontar, E. P., Chen, X., Chrysaphi, N., et al. 2019, *ApJ*, **884**, 122
 Kouloumvakos, A., Rouillard, A., Warmuth, A., et al. 2021, *ApJ*, **913**, 99
 Krafft, C., & Volokitin, A. S. 2016, *ApJ*, **821**, 99
 Krafft, C., & Volokitin, A. 2017, *J. Plasma Phys.*, **83**, 705830201
 Krafft, C., Volokitin, A. S., & Krasnoselskikh, V. V. 2013, *ApJ*, **778**, 111
 Krafft, C., Volokitin, A. S., Krasnoselskikh, V. V., & de Wit, T. D. 2014, *J. Geophys. Res. (Space Phys.)*, **119**, 9369
 Krafft, C., Volokitin, A. S., & Krasnoselskikh, V. V. 2015, *ApJ*, **809**, 176
 Krasnoselskikh, V. V., Kruchina, E. N., Volokitin, A. S., & Thejappa, G. 1985, *A&A*, **149**, 323
 Krasnoselskikh, V., Voshchepynets, A., & Maksimovic, M. 2019, *ApJ*, **879**, 51
 Krupar, V., Eastwood, J. P., Kruparova, O., et al. 2016, *ApJ*, **823**
 Krupar, V., Maksimovic, M., Kontar, E. P., et al. 2018, *ApJ*, **857**, 82
 Krupar, V., Szabo, A., Maksimovic, M., et al. 2020, *ApJS*, **246**, 57
 Kundu, M. R. 1965, *Solar Radio Astronomy* (Interscience Publishers)
 Leblanc, Y., Dulk, G. A., & Bougeret, J.-L. 1998, *Sol. Phys.*, **183**, 165
 Ledenev, V. G., Zverev, E. A., & Starygin, A. P. 2004, *Sol. Phys.*, **222**, 299
 Li, B., Cairns, I. H., & Robinson, P. A. 2012, *Sol. Phys.*, **279**, 173
 Magdalenic, J., Vršnak, B., Zlobec, P., Hillaris, A., & Messerotti, M. 2006, *ApJ*, **642**, L77
 Magdalenic, J., Marqué, C., Zhukov, A. N., Vršnak, B., & Žic, T. 2010, *ApJ*, **718**, 266
 Magdalenic, J., Marqué, C., Krupar, V., et al. 2014, *ApJ*, **791**, 115
 Magdalenic, J., Marqué, C., Fallows, R. A., et al. 2020, *ApJ*, **897**, L15
 Mann, G., Vocks, C., & Warmuth, A. 2022, *A&A*, **660**, A91
 Martínez Oliveros, J. C., Raftery, C. L., Bain, H. M., et al. 2012, *ApJ*, **748**, 66
 McLean, D. J., & Labrum, N. R. 1985, *Solar Radiophysics: Studies of Emission from the Sun at Metre Wavelengths* (Cambridge University Press)
 Melnik, V. N., Brazhenko, A. I., Frantsuzenko, A. V., Dorovskyy, V. V., & Rucker, H. O. 2018, *Sol. Phys.*, **293**, 26
 Melnik, V. N., Konvalenko, A. A., Yerin, S. M., et al. 2019, *ApJ*, **885**, 78
 Melnik, V. N., Brazhenko, A. I., Konvalenko, A. A., et al. 2021, *Sol. Phys.*, **296**, 9
 Müller, D., Marsden, R. G., & St. Cyr, O. C., & Gilbert, H. R., 2013, *Sol. Phys.*, **285**, 25
 Neugebauer, M. 1975, *J. Geophys. Res.*, **80**, 998
 Pulupa, M., Bale, S. D., Badman, S. T., et al. 2020, *ApJS*, **246**, 49
 Reid, H. A. S., & Ratcliffe, H. 2014, *Res. Astron. Astrophys.*, **14**, 773
 Reid, H. A. S., & Kontar, E. P. 2021, *Nat. Astron.*, **5**, 796
 Sanchez-Diaz, E., Rouillard, A. P., Davies, J. A., et al. 2017, *ApJ*, **835**, L7
 Sawant, H. S., Degaonkar, S. S., Alurkar, S. K., & Bhonsle, R. V. 1978, *Bull Astron. Soc. India*, **6**, 52
 Sharykin, I. N., Kontar, E. P., & Kuznetsov, A. A. 2018, *Sol. Phys.*, **293**, 115
 Spangler, S. R. 2002, *ApJ*, **576**, 997
 Suzuki, S., & Dulk, G. A. 1985, in *Solar Radiophysics: Studies of Emission from the Sun at Metre Wavelengths*, eds. D. J. McLean, & N. R. Labrum (Cambridge University Press) 289
 Tkachenko, A., Krasnoselskikh, V., & Voshchepynets, A. 2021, *ApJ*, **908**, 126
 van Haarlem, M. P., Wise, M. W., Gunst, A. W., et al. 2013, *A&A*, **556**, A2
 Voshchepynets, A., & Krasnoselskikh, V. 2015, *J. Geophys. Res. (Space Phys.)*, **120**(10), 139
 Voshchepynets, A., Krasnoselskikh, V., Artemyev, A., & Volokitin, A. 2015, *ApJ*, **807**, 38
 Zhang, P., Zucca, P., Sridhar, S. S., et al. 2020, *A&A*, **639**, A115
 Zucca, P., Carley, E. P., Bloomfield, D. S., & Gallagher, P. T. 2014, *A&A*, **564**, A47